J. Biomechanics Vol. 20, No. 3, pp. 261–270, 1987.
Printed in Great Britain

0021-9290/87 $3.00 + .00

ELECTROMECHANICAL POTENTIALS IN CORTICAL BONE—I. A CONTINUUM APPROACH

RICHARD A. SALZSTEIN*‡, SOLOMON R. POLLACK*, ARTHUR F. T. MAK* and NIKOLA PETROV

*Department of Bioengineering, University of Pennsylvania, Philadelphia, PA, U.S.A. †Institute of Mechanics and Biomechanics, Bulgarian Academy of Sciences, Sofia, Bulgaria

Abstract An electrokinetic model to characterize the electromechanical effect in cortical bone has been developed using the basic principles of the biphasic theory of porous materials and a simple model for permeability and charge distribution for cortical bone. The model is developed analytically in Part I of this paper and is shown to account qualitatively for the principal experimental results reported to date. Part II of this paper concerns experimental analysis of this model, reporting results of low frequency testing of the dynamic characteristics of stress-generated potentials. Quantitative analysis of these results indicates that the microporosity of bone, made up of the channels around the hydroxyapatite encrusting the collagen matrix, is the compartment responsible for the electromechanical effects in fluid-saturated cortical bone. This microporous compartment would seem to be the obvious source of the electrokinetic effect, because it has the greatest surface area in bone and constitutes the rate limiting fluid flow compartment in deformation-induced fluid flow at low frequency.

NOMENCLATURE

a_{11}	hydraulic permeability
a_{12}, a_{21}	electromechanical coupling coefficients
a_{22}	conductivity
c	1/2 plate width
$C^l(r)$, C^l_0	concentration of species l; at radius r in channel, in bulk, respectively
e	trace of ε
f	strain ε_{yy}
g, G	(radius of curvature of plate)$^{-1}$
h	1/2 plate thickness
H_A	aggregate modulus
i	$\sqrt{-1}$
$\mathbf{I}$	identity tensor
I_0, I_2	modified Bessel functions
j_c	convective current per channel
J_c	total convective current
J_T	total current
k	permeability
k_B	Boltzmann's constant
K	dissipative drag coefficient
M	moment
n	number of channels per unit area
P	pressure
$\mathbf{Q}$	volume flow rate
R	characteristic channel radius
t	time
T	tortuosity
T_A	absolute temperature
$\mathbf{u}$	displacement tensor of solid
$\mathbf{v}^s$, $\mathbf{v}^f$	velocity tensors of solid and fluid, respectively
$v_y(r)$	fluid flow at radius r in channel
V	electrical potential
V_s, V_{SGP}	streaming potential and stress generated potential, respectively
x, y, z	rectangular coordinates
z^l	valence of ion species l
Z	zeta potential
γ	complex wave number
$\Gamma_{l/g}$, Γ_c	surface tensions; liquid/gas and critical, respectively
δ	characteristic channel diameter
ε	dielectric permittivity of fluid
$\boldsymbol{\varepsilon}$	strain tensor of solid
η	fluid viscosity
κ^{-1}	Debye length
λ_s, μ_s	Lamé constants of elastic solid matrix
ν	Poisson's ratio of elastic solid matrix
$\rho(r)$	charge density at radius r in channel
$\boldsymbol{\sigma}^s$, $\boldsymbol{\sigma}^f$	stress tensor in solid and fluid, respectively
σ, σ_b	conductivity of fluid and porous plate (bone), respectively
τ_n	time constant
ϕ^s, ϕ^f	volume fraction of solid and fluid, respectively
$\psi(r)$	potential at radius r in channel
ω	driving frequency
$\dot{(\ )}$	time derivative
$(\ )_{,x}$	partial derivative with respect to x
$\tilde{(\ )}$	non-dimensional quantity

Received 30 *August* 1985; *in revised form* 8 *July* 1986.

‡Present address: Hercules Incorporated, Wilmington, DE 19894, U.S.A.

INTRODUCTION

Bone will produce electrical potentials when subjected to deformation. These electromechanical potentials, often referred to as stress-generated potentials (SGPs), have been demonstrated both *in vivo* and *in vitro*, under a variety of conditions since first reported by Yasuda (1953). The role of these potentials in bone growth, remodelling and repair has received much speculation, though the actual physiological significance of this phenomenon has not been demonstrated.

This paper describes a model for the generation of these potentials. Two basic mechanisms have been suggested for the origin of these potentials in fluid-filled bone; piezoelectricity and electrokinetics (Anderson and Eriksson, 1968). This work describes a model for the electrokinetic origin of these signals, indicating that in fluid-filled bone, this mechanism accounts for the principal experimental findings reported to date.

Electrokinetic effects result when a relative velocity exists between a polar fluid and charged surface. The fluid in bone exists in three characteristic regions: the vascular structures (Haversian and Volkmann's canals), osteocytic or lacunar spaces and their associated canaliculi, and the microporous spaces made up of the pathways around the mineral hydroxyapatite encrusting the collagen structure. The relative size of these spaces has been reported previously (Holmes *et al.*, 1964). At low frequencies, the rate-limiting fluid flow is through the microporous channels (Johnson, 1984). Since these microporous spaces have the largest surface area in bone (Neuman and Neuman, 1958), these spaces will dominate electrokinetic effects, at low frequencies. Previous workers have reported the existence of a nonzero zeta potential in bone. Therefore, the fluid in bone must be characterized by polar double layer regions that will give rise to streaming potentials when fluid flow occurs. This model will deal specifically with strain-induced flow in this microporous region and the resulting electrokinetic potentials that can be observed macroscopically.

The microporosity is taken to constitute a two-phase continuum for modelling the electromechanical effect, neglecting, therefore, the vascular structures of bone and the lacunar and canalicular spaces. Utilizing the basic principles developed in the biphasic theory of porous materials by Mow and co-workers (Mow *et al.*, 1980; Mow and Lai, 1980), the pressure in the fluid can be determined throughout the specimen. A micro-continuum model (Grodzinsky, 1983) for charge distribution within the micropores together with the first principles of electrokinetic theory then enable the determination of electrokinetic potentials for a given set of boundary conditions. Thus, the model determines the strain-induced flow of fluid in the microporous spaces of cortical bone and the resulting electrokinetic potentials. The model is then compared to most of the previous experimental reports on SGPs.

Bone is a viscoelastic tissue, as are most other tissues in the body (Lakes and Katz, 1984). The viscoelastic response of bone must be addressed in any dynamic treatment of mechanics of cortical bone. The methods we employ here begin to account for this viscoelastic response at low frequencies as a poroelastic mechanism in an elastic, calcified collagen matrix. This approach has been effective in accounting for cartilage mechanics, where the collagenous matrix is not calcified and is even more prone to nonelastic effects (Mow *et al.*, 1980; Lee *et al.*, 1981). We must also recognize that bone is nonisotropic and inhomogeneous, though this early model considers an isotropic, homogeneous calcified collagenous matrix, with equal compressive and tensile moduli.

The biphasic analysis that we employ here considers an inviscid fluid fraction and determines the fluid pressure throughout the specimen. Viscous terms in the biphasic analysis are considered to have a small effect on the pressures and, as such, are neglected in determining pressure. Real fluids used in actual experimentation will be viscous. We will assume that the viscous nature of the fluid can be modelled on the micro-continuum level, where the effect on charged solid surfaces and their interfaces with polar liquids are considered. In this manner, the viscosity of the solution will be accounted for in the permeability of the porous material.

THEORY

Previous work in this field has studied the SGPs developed by bending fluid-filled machined slabs of cortical bone. The development here is for pure bending of these *in vitro* specimens. The model begins by utilizing the biphasic constitutive equations to determine the space-time dependence of the fluid pressure during dynamic loading. The micro-continuum model is then developed to relate the convective current density to the pressure gradient in the fluid and to the electrical double layer properties. Electrokinetic theory then permits the determination of the streaming potentials, or SGPs, by integration of the pressure gradient after determining the electrokinetic coefficients.

Biphasic analysis

Consider the bending of the porous-elastic plate shown in Fig. 1. The plate is taken as homogeneous and isotropic with thickness $2h$ and width $2c$ and is subjected to pure bending. The neutral plane is along $y = 0$. The surface $y = +h$ is under maximum compression and the surface $y = -h$ is under maximum tension. We consider an elastic matrix and an inviscid fluid-filled porous fraction. Both phases are considered incompressible. From the linear biphasic theory (Mow and Lai, 1980), the constitutive equations for the solid and fluid phases are, respectively,

$$\boldsymbol{\sigma}^s = -\phi^s P\mathbf{I} + \lambda_s e\mathbf{I} + 2\mu_s \boldsymbol{\varepsilon} \tag{1}$$

$$\boldsymbol{\sigma}^f = -\phi^f P\mathbf{I}. \tag{2}$$

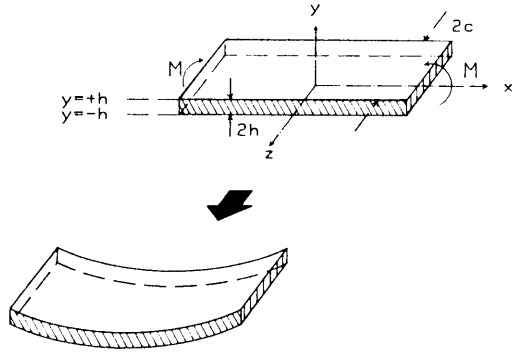

Fig. 1. Pure bending sample geometry, indicating porous plate thickness $2h$ and width $2c$. The plate, composed of an elastic solid matrix and a fluid-filled porous fraction, is subjected to bending deformations, resulting in bending moments M.

$P = P(y, t)$ is the pressure in the fluid relative to the pressure in its equilibrium (unstrained) state, λ_s and μ_s are the Lamé constants of the elastic bone matrix, and ϕ^s and ϕ^f represent the volume fractions of the solid and fluid phases, respectively. We neglect the viscous nature of the fluid, as its contribution in determining the pressure is small (Armstrong *et al.*, 1984). Since both phases are considered incompressible, they are mutually exclusive and fluid must flow out of regions of compression of the solid matrix and into regions of dilatation. The equation of continuity is

$$\nabla \cdot (\phi^s \mathbf{v}^s + \phi^f \mathbf{v}^f) = 0, \tag{3}$$

$\mathbf{v}^s$ and $\mathbf{v}^f$ are the velocities of the solid and fluid, respectively. $\mathbf{v}^s$ is the time derivative of the displacements, $\mathbf{u}$, of the solid. For slow relative displacements of the two phases, the inertia of the system is taken to be small relative to the energy dissipated by the drag of one phase moving relative to the other. The equation of equilibrium for the two phases becomes

$$\nabla \cdot \sigma^s + K(\mathbf{v}^f - \mathbf{v}^s) = 0 \tag{4}$$

$$\nabla \cdot \sigma^f + K(\mathbf{v}^s - \mathbf{v}^f) = 0. \tag{5}$$

Here, K represents the dissipative drag coefficient.

For the specific geometry of the plate, plane strain dictates that there are no dependencies in the z-direction, so that the derivative of all quantities with respect to z is zero. Also, we consider no shearing strains in the plate. The imposed deformation of elastic solid matrix in the x-direction causes a Poisson-type reaction in the y-direction, analogous to the work of Armstrong *et al.* (1980). Imposing a state of pure bending

$$\varepsilon_{xx} = -yg(t) \tag{6}$$

where $g(t)$ contains the driving mode of deformation with time t and has the units of length^{-1} (inverse of the radius of curvature of the plate). The bending deformation and the associated fluid flow will cause a normal strain in the matrix in the y-direction

$$\varepsilon_{yy} = f(y, t). \tag{7}$$

Small matrix strains will have little effect on the relative solid and fluid fractions, such that $\partial\phi^s/\partial x_i = 0$ and $\partial\phi^f/\partial x_i = 0$.

With the strain deformation relationship of the solid matrix

$$\varepsilon_{ij} = \frac{1}{2}\left(\frac{\partial u_i}{\partial x_j} + \frac{\partial u_j}{\partial x_i}\right) \tag{8}$$

the terms in the equation of continuity are

$$v^s_{x,x} = v^f_{x,x} = \dot{\varepsilon}_{xx} = -y\dot{g} \tag{9}$$

$$v^s_{y,y} = \dot{\varepsilon}_{yy} = \dot{f}. \tag{10}$$

The terms $v^s_{x,x}$ and $v^f_{x,x}$ are the derivatives in the x-direction of the x-component of the velocity of the solid and fluid, respectively. Similarly, the term $v^s_{y,y}$ is the derivative in the y-direction of the y-component of the velocity of the solid. $\dot{}$ denotes the derivative with respect to time. Due to symmetry, one can impose that the two phases do not move relative to one another in the x-direction, as indicated in equation (9). Solving for $v^f_{y,y}$ from equation (3) using equations (8), (9) and (10)

$$v^f_{y,y} = \frac{1}{\phi^f}(y\dot{g} - \phi^s\dot{f}). \tag{11}$$

Equating the y-components of the equation of equilibrium of the two phases (equations 4 and 5),

$$\sigma^s_{yy,y} = -\sigma^f_{yy,y} \tag{12}$$

and using the stress–strain relations of equations (1) and (2) and expressions for strain equations (6) and (7)

$$P_{,y} = H_A f_{,y} - \lambda_s g \tag{13}$$

where $H_A = 2\mu_s + \lambda_s$ is the aggregate modulus of the elastic matrix (Mow and Lai, 1980). Taking the derivative in the y-direction of equation (13) yields

$$P_{,yy} = H_A f_{,yy}. \tag{14}$$

If we differentiate equation (5) with respect to y and utilize the constitutive equation (2) and the gradient of the fluid velocity given by equations (10) and (11), we obtain

$$P_{,yy} = \frac{1}{k}(\dot{f} - y\dot{g}) \tag{15}$$

where $k = (\phi^f)^2/K$ is the permeability of the matrix (Mow and Lai, 1980). This permeability is modeled in the latter portion of this development to account for the microporosity of the cortical bone matrix. Thus, the governing equation for this approach is obtained by setting equations (14) and (15) equal

$$f_{,yy} = \frac{1}{H_A k}(\dot{f} - y\dot{g}) \tag{16}$$

Electromechanical potentials have traditionally been measured under a step-load or sinusoidal deformation mode. Here, we consider the steady state solution of this partial differential equation for sinusoidal deformation: $g(t) = G\exp(i\omega t)$, where G is related to the magnitude of the driving deformation.

The boundary conditions are considered as follows. For a specimen immersed in a shallow fluid bath, where the hydrodynamic pressure is taken to be zero, a free-flow condition at the surfaces $y = \pm h$ dictates the boundary condition

$$P(\pm h, t) = 0. \tag{17}$$

The steady state solution for the normal strain ε_{yy} is determined by solving equation (16) for $f(y, t)$, with the conditions of free-flow and the stress-free surfaces ($y = \pm h$)

$$\varepsilon_{yy} = f(y, t) = \left\{y - \frac{2\mu_s h}{H_A}\left[\frac{\sinh(\gamma y/h)}{\sinh(\gamma)}\right]\right\} Ge^{i\omega t} \tag{18}$$

where γ is the complex wave number

$$\gamma = (1 + i)\left(\frac{\omega h^2}{2H_A k}\right)^{1/2}. \tag{19}$$

The neutral plane ($y = 0$) is free of normal strains which will result in zero pressure in the fluid on the neutral plane. The resulting pressure is an odd function about $y = 0$

$$P(y, t) = 2\mu_s\left[y - \frac{h\sinh(\gamma y/h)}{\sinh(\gamma)}\right]Ge^{i\omega t}. \quad (20)$$

We may also consider the case when the specimen is placed in a humidity chamber. This has been the type of measurement most frequently employed. In this case, the fluid is not free to drain from the porous spaces, because surface tension may keep the fluid from freely exposing unwetted surfaces of the matrix (Johnson, 1984). The maximum surface tension attainable is inversely proportional to the diameter of the pore size. With pore diameters estimated at 200–600 Å (Holmes *et al.*, 1964), large pressures due to surface tension may dictate a zero pressure gradient boundary condition

$$P_{,y}(\pm h, t) = 0. \quad (21)$$

The pressures on the boundaries $y = \pm h$ must be smaller than the maximum attainable pressure due to surface tension (Moore, 1972)

$$P_{\text{surface tension}} = 4\,\Gamma_{l/g}/\delta \quad (22)$$

where $\Gamma_{l/g}$ is the surface tension of the fluid and δ is the characteristic diameter of the matrix porosity. With this zero pressure gradient condition at the surfaces $y = \pm h$, we can again determine the normal strain ε_{yy}, considering the conditions imposed by equation (13)

$$\varepsilon_{yy} = f(y, t) = \left\{y - \frac{2\mu_s h}{H_A\gamma}\left[\frac{\sinh(\gamma y/h)}{\cosh(\gamma)}\right]\right\}Ge^{i\omega t} \quad (23)$$

and obtain the pressure within the specimen

$$P(y, t) = 2\mu_s\left[y - \frac{h\sinh(\gamma y/h)}{\gamma\cosh(\gamma)}\right]Ge^{i\omega t}. \quad (24)$$

The zero-pressure gradient condition (equation 21) is considered in the remaining portion of this development, since this should reflect the boundary conditions for electromechanical testing of samples *not* immersed in fluid while testing. With this condition, the resulting stress in the matrix (equation 1) may be integrated over the product of the moment arm y and the cross-sectional element of the plate to determine the resulting dynamic moment of the deformation of the sample

$$M(t) = 2c\int_{-h}^{h} y\sigma_{xx}^{T}\,dy = 16\mu_s ch^3\left\{\frac{1}{3} + \frac{\mu_s}{H_A\gamma^2}\left[\frac{\tanh(\gamma)}{\gamma} - 1\right]\right\}Ge^{i\omega t}. \quad (25)$$

Micro-continuum model for charge distribution, permeability, and convective current

To this point in the development, continuum parameters have been used to describe the strains and pressures resulting from deformation of the porous-elastic plate. To consider electrokinetic effects, specifically streaming potentials in this case, polar fluids must move relative to charged surfaces. We model a micro-continuum, following Grodzinsky (1983), to account for these surfaces within our continuum framework, determine a distribution of charges within this micro-continuum and then account for electrokinetic phenomena on the basis of a simple model for the permeability of cortical bone and the driving pressures derived in the previous section.

An electric double layer will form at the interface of a polar liquid and a charged solid surface. The surface charge and the ion concentration in the fluid influence the distribution of the ions in the polar liquid. Electrochemical attraction of one ionic species to the surface will result in a spatially decaying potential in the fluid. If the fluid space is large compared with the Debye length, the potential will decay to zero in the bulk of the fluid. The zeta potential is the potential at the slip plane in the fluid. Inside the slip plane, fluid is not free to move, but is bound to the interface with the solid. The zeta potential is influenced by several factors, including the geometry of the surface, the concentration of each ion species in solution, the presence or absence of absorbed species at the interface and the location of the hydrodynamic slip plane. The Poisson–Boltzmann equation describes the decay of the potential and charge density from the slip plane to the bulk of the fluid where the net charge density approaches zero. The electric double layer contains the fluid region located several tens of Angstroms from the interface and it contains much of the mobile charge.

We consider an idealized cylindrical pore with an axisymmetric charge distribution within the pore (Pollack *et al.*, 1984). The linear Poisson–Boltzmann equation is used to describe the radial decay of potential $\psi = \psi(r)$ from the position $r = R$ (at radius of the slip plane) to $r = 0$ at the center of the pore

$$\nabla^2\psi(r) = \kappa^2\psi(r) = -\frac{\rho(r)}{\varepsilon}. \quad (26)$$

Charge neutrality is assumed at the center of the channel. κ^{-1} is the Debye length, defined such that

$$\kappa^2 = \frac{e^2}{\varepsilon k_B T_A}\sum_l (z^l)^2 C_0^l \quad (27)$$

where e is the charge on an electron, z^l is the valence of the lth ion type, C_0^l is equilibrium concentration of the lth species at the center of the channel, ε is the dielectric permittivity of the fluid (assumed constant here), k_B is Boltzmann's constant, and T_A is the absolute temperature. The summation is over all ionic species. $\rho = \rho(r)$ is the charge density in the fluid

$$\rho(r) = \sum_l z^l e C^l(r) \quad (28)$$

where $C^l(r)$ is the concentration of the lth species at radius r.

Following Pollack *et al.* (1984), the radial component of equation (26) is the modified Bessel equation

of order zero. With the boundary conditions such that the potential is equal to the zeta potential at the slip plane and finite at the center of the fluid channel

$$\psi(R) = Z \qquad (29)$$

$$\psi(0) \quad \text{finite}$$

the solution of the radial component of equation (26) is

$$\psi(r) = Z\frac{I_0(\kappa r)}{I_0(\kappa R)} \qquad (30)$$

and

$$\rho(r) = -\kappa^2 \varepsilon Z\frac{I_0(\kappa r)}{I_0(\kappa R)}. \qquad (31)$$

Fluid flow outside the slip plane will carry a net charge, causing a convective (streaming) current flow downstream within the channel. In the biphasic analysis considered here, the fluid fraction is taken to be inviscid, as viscous properties will have small effect on the pressures developed. The permeability in the biphasic approach is described in terms of this *inviscid* fluid fraction. However, we introduce the viscosity at the micro-continuum level in order to account for the fluid flow profile resulting from pressure gradients and to model the permeability more realistically. It is this model of permeability that will be incorporated into the biphasic model of the driving pressure (equation 24).

In models of porous media, Darcy's law describes the volume flow rate per unit cross section (**Q**) of the material as a function of the permeability (k) and the pressure gradient

$$\mathbf{Q} = -k\nabla P. \qquad (32)$$

Scheidegger (1974) gives a simple model for permeability for a fluid of viscosity η in a porous material composed of tortuous channels

$$k = \frac{\phi^f \delta^2}{96\eta T^2} \qquad (33)$$

where $\delta = 2R$ is the characteristic or average diameter of the channels of the porous material and T is the channel tortuosity, the ratio of the path length through each channel to the net distance traversed. The model is derived for n channels per unit area

$$n = \frac{4\phi^f}{3\pi\delta^2 T} \qquad (34)$$

where the channels traverse the material in each spatial direction. For a cubic sample of unit volume of the porous material, each channel is taken to originate on one surface of the cube and terminate on the opposite side. The volume of the flow channels constitutes the entire fluid fraction of the material.

To model the nature of the electric double layer in these channels and the resulting convective current, we consider a parabolic velocity profile, $v_y(r)$, in each tortuous channel

$$v_y(r) = \left(\frac{r^2 - R^2}{4\eta T}\right) P_{,y}. \qquad (35)$$

The convective current in each channel, j_c, is then the product of the velocity, $v_y(r)$, and the charge density, $\rho(r)$, integrated over the channel area

$$j_c = \int_0^R v(r)\rho(r)2\pi r dr = \frac{Z\varepsilon\pi R^2}{\eta T}\left[\frac{I_2(\kappa R)}{I_0(\kappa R)}\right] P_{,y}. \qquad (36)$$

The convective current density, J_c, is then the product of convective current in each channel, j_c, and the number of channels per unit area, n

$$J_c = \frac{Z\varepsilon\phi^f}{3\eta T^2}\left[\frac{I_2(\kappa R)}{I_0(\kappa R)}\right] P_{,y}. \qquad (37)$$

Electrokinetic analysis

In the presence of the convective current, a downstream potential difference exists, causing a reverse conduction current. Steady state is reached when these two currents are equal and opposite and no further net charge is transported. The electrical potential that exists at this steady state condition is the streaming potential, V_s. In classical electrokinetic theory for flow of fluid in a single straight channel through a solid material (Shaw, 1969), V_s is determined by the fluid conductivity σ, viscosity η, and dielectric permittivity ε, the zeta potential Z, and the pressure-inducing fluid flow

$$V_s = \frac{Z\varepsilon P}{4\pi\sigma\eta}. \qquad (38)$$

Grodzinsky (1983) considers a continuum approach to model electrokinetic transport. For our geometry and homogeneous, isotropic conditions, equations (39) and (40) describe Q_y, the volume flow rate in the y-direction per unit area, and J_T, the total current density, resulting from pressure and voltage gradients (Lee *et al.*, 1981)

$$Q_y = -a_{11}P_{,y} + a_{12}V_{,y} \qquad (39)$$

$$J_T = a_{21}P_{,y} - a_{22}V_{,y}. \qquad (40)$$

In the absence of a voltage gradient, equation (39) reduces to Darcy's law, and a_{11} is the hydraulic permeability of the material. In the absence of a pressure gradient, J_T in equation (40) is purely a conductive current, indicating that a_{22} is the electrical conductivity of the material. a_{12} and a_{21} are the electrokinetic coefficients associated with the material. The Onsager reciprocity theorem indicates that these two coefficients are equal: $a_{12} = a_{21}$. a_{21} is given as the coefficient of the pressure gradient in equation (37).

Four electrokinetic phenomena are then defined by equations (39) and (40), including streaming potentials, streaming currents, electroosmosis and electroosmotic pressures (Grodzinsky, 1983). Here, we are interested in the streaming potentials where J_T is zero. This is equivalent to setting the convective and conductive currents equal and opposite so that no net transfer occurs in steady state.

The voltage profile across the sample is found by integrating equation (40), with $J_T = 0$, from $y = 0$ to the y-position of interest. The voltage and pressure at

the neutral axis of bending ($y = 0$) are zero

$$V(y,t) = \frac{a_{21}}{a_{22}} P(y,t). \tag{41}$$

The voltage difference between the tension and compression sides is evaluated from equation (41) for $y = \pm h$, using the fact that $P(y,t)$ is an odd function about $y = 0$

$$V(-h,t) - V(+h,t) = \frac{-2a_{21}}{a_{22}} P(h,t). \tag{42}$$

The expression for a_{21} is given by equation (37). Taking $a_{22} = \sigma_b$ (the conductivity of bone) and the expression for the pressures from equation (24), the SGP voltage difference across the sample is

$$V_{SGP} = \frac{4\mu_s Z e \phi^1}{3\eta\sigma_b T^2}\left[\frac{I_2(\kappa R)}{I_0(\kappa R)}\right]\left[\frac{\tanh(\gamma)}{\gamma} - 1\right] Ghe^{i\omega t}. \tag{43}$$

RESULTS

The model developed in the previous section has many interesting implications, both mechanically and electromechanically. We will first consider the mechanical indications and determine the dynamic characteristics of the poroelastic relaxation mechanism analyzed for an elastic approximation of the calcified matrix of cortical bone. The electromechanical results are then considered and the predicted dynamic characteristics of stress-generated potentials are presented. The dynamic response has been determined experimentally and is discussed in the second part of this paper (Salzstein and Pollack, 1985). Many other experimental findings of SGPs are related to this model; they are considered in the Discussion section of this paper.

Mechanical results

We have described two types of boundary conditions that need to be considered in the analysis of a pressure profile across the sample. The first type of condition is a free-flow condition at the surfaces $y = \pm h$, which may occur if the sample is tested while immersed in a fluid bath. Under these conditions, the fluid is free to flow in and out of the sample and the boundary condition described in equation (17) is applicable. An analysis of equation (20) allows the determination of the pressure profile across the sample using the following non-dimensional parameters

$$\tilde{y} = y/h; \quad \tilde{t} = \frac{tH_A k}{h^2}; \quad \tilde{\omega} = \frac{\omega h^2}{H_A k}; \quad \tilde{P} = \frac{P}{2\mu_s G h}. \tag{44}$$

The complex wave number, γ, is then

$$\gamma = (1+i)\left(\frac{\tilde{\omega}}{2}\right)^{1/2} \tag{45}$$

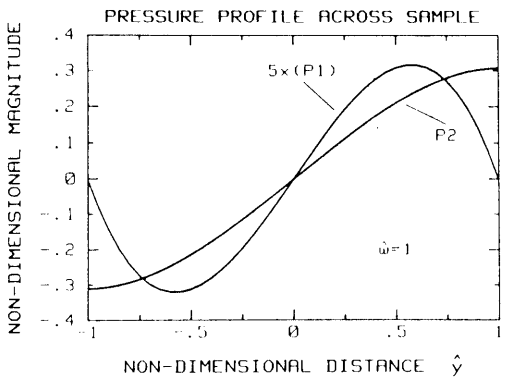

Fig. 2. Non-dimensional pressure profiles across the bending sample for $\tilde{\omega} = 1$, predicted by equations (46) and (47), for the two types of boundary conditions: free-flow boundary (curve $P1$) and no-flow boundary (curve $P2$), respectively. The curve $P1$ has been multiplied by a factor of five for presentation purposes only.

and we obtain

$$\tilde{P} = \left[\tilde{y} - \frac{\sinh(\gamma\tilde{y})}{\sinh(\gamma)}\right]. \tag{46}$$

The non-dimensional pressure profile $\tilde{P}$, across the specimen, is shown in Fig. 2, for $\tilde{\omega} = 1$. The sign of the magnitude of the pressure is maintained in the figure, and this indicates positive pressures on the compressive side ($\tilde{y} > 0$) and negative pressures on the tensile side ($\tilde{y} < 0$). (In Fig. 2, the curve '$P1$' represents the free-flow condition and the amplitude is multiplied by a factor of five for presentation purposes only.) Under this free-flow condition, no net pressure gradient exists across the entire specimen and no net transport of fluid occurs. As a result, no net electrokinetic potential across the entire specimen is predicted (Johnson, 1984).

If we next consider the boundary condition of equation (21), where effects of surface tension may dictate no net flow through the surfaces $y = \pm h$, non-dimensionalizing the pressure profile solution of equation (24) reveals

$$\tilde{P} = \left[\tilde{y} - \frac{\sinh(\gamma\tilde{y})}{\gamma\cosh\gamma}\right] \tag{47}$$

and this is also shown in Fig. 2, labeled '$P2$'. In this case, a net pressure gradient does exist and a net transfer of fluid and charge will occur from the compression to the tensile side of the bending specimen (Johnson, 1984). As $\tilde{\omega}$ is increased, the net pressure difference across the sample is increased. This pressure difference between the tensile and compressive surfaces asymptotically approaches 2 on the scale shown in Fig. 2, with increasing $\tilde{\omega}$.

Considering either the free-flow case or the zero-gradient case, the total stress normal to the surfaces at $y = \pm h$ is zero, as expected for unconstrained surfaces.

Equation (25) describes the dynamic moment resulting from the sinusoidal deformation, $g(t)$. Using standard relationships among the elastic constants and

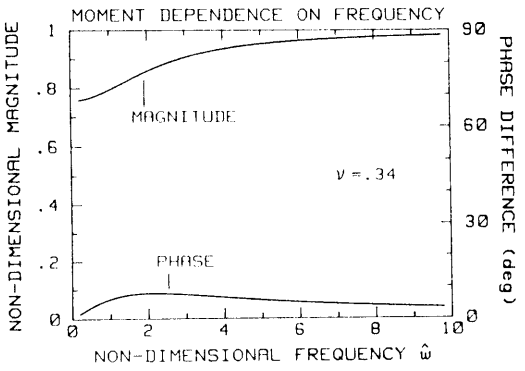

Fig. 3. Non-dimensional magnitude and phase of the moment dependence on driving frequency $\hat{\omega}$. This curve was predicted by equation (48), for a value of $\nu = 0.34$. Over one decade of non-dimensional frequency, $\hat{\omega}$, the magnitude of the predicted induced moment from the driving bending deformation increases monotonically, on the order of 20%. Small phase angles ($< 10^\circ$) are shown.

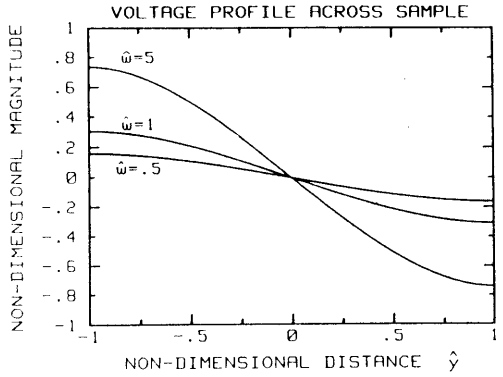

Fig. 4. Predicted non-dimensional voltage profile across sample from equation (49), for various values of $\hat{\omega}$.

non-dimensionalizing,

$$\hat{M} = \frac{3M}{16\mu_s ch^3 G} = \left\{1 + \frac{3(1-2\nu)}{2(1-\nu)\gamma^2}\left[\frac{\tanh(\gamma)}{\gamma} - 1\right]\right\}. \tag{48}$$

Figure 3 illustrates the magnitude of the moment as a function of $\hat{\omega}$, increasing approximately 20% for $\nu = 0.34$ (Poisson's ratio of the elastic solid), over one decade of dimensionless frequency, as shown. The corresponding phase (relative to the driving deformation) of the moment is also shown, with a maximum phase of approximately 7°, decaying with increasing $\hat{\omega}$ beyond $\hat{\omega} = 2$. Thus, the poroelastic mechanism modeled here *may* account for a portion of the nonelastic effects found in cortical bone (Lakes and Katz, 1984).

Electromechanical results

The non-dimensional magnitude of the voltage profile, $\tilde{V}$, across the sample is obtained from equations (41), (47) and (49) and, for negative zeta potentials typically found for bone (Eriksson, 1976), is given by

$$\tilde{V} = \frac{Va_{22}}{2a_{21}\mu_s Gh} = \left[\frac{\sinh(\gamma\hat{y})}{\gamma\cosh(\gamma)} - \hat{y}\right]. \tag{49}$$

Figure 4 illustrates equation (49) for various values of $\hat{\omega}$. Figure 5 illustrates the frequency dependence of the voltage difference from one side of the specimen to the other, obtained by non-dimensional analysis of equation (43)

$$\tilde{V}_{SGP} = V_{SGP}\left[\frac{3\eta\sigma_b T^2}{4\mu_s Zc\phi^2 Gh}\right]\left[\frac{I_0(\kappa R)}{I_2(\kappa R)}\right]. \tag{50}$$

Again, for a negative value for the zeta potential, $\tilde{V}_{SGP}$ becomes

$$\tilde{V}_{SGP} = \left[1 - \frac{\tanh(\gamma)}{\gamma}\right]. \tag{51}$$

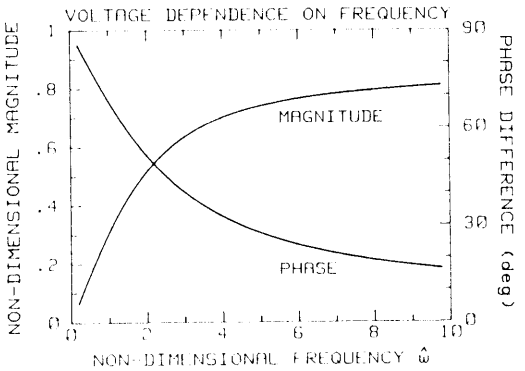

Fig. 5. Predicted non-dimensional magnitude and phase of the voltage difference across the bending sample as a function of $\hat{\omega}$, from equation (51). The magnitude monotonically increases and the phase monotonically decreases from 90° over the frequency range shown.

The voltage difference across the sample asymptotically approaches a value of 1 with increasing $\hat{\omega}$. The phase of the voltage difference is also shown in Fig. 5, decreasing rapidly from 90° at small values of $\hat{\omega}$.

DISCUSSION

A model characterizing an electrokinetic origin for stress-generated potentials in cortical bone has been formulated, treating bone as a continuum, neglecting any specific architecture of the tissue. The theory is subject to several limitations which are discussed below. Following this, a discussion of several functional dependencies exhibited by the model is presented, considering the principal experimental results of SGPs reported in the literature for fluid-filled bone.

Limitations of the model

We must first recognize that cortical bone does indeed have a microstructure, composed of the vas-

cular and cellular structures. A previous paper addressed the development of intraosteonal SGPs (Pollack *et al.*, 1984). Our model of a continuum for bone considers bone as a homogeneous, isotropic permeable porous body composed of an elastic matrix and a mobile fluid fraction. The viscoelastic properties of the matrix are neglected.

We have neglected the effect that the viscous nature of the fluid will have on the development of the pressures within the porous body. This assumption should be sufficient at low driving frequencies and low viscosities where the acceleration of the fluid and its viscous effects will be minimal. These low frequencies are defined such that the electrokinetic steady state condition is established at frequencies much higher than the low driving frequencies (Johnson *et al.*, 1980).

Pollack *et al.* (1984) described a model for stress-generated potentials developed within osteons. The limitations of that model, concerning the development of a similar micro-continuum, will apply here. These limitations include: (1) the application of the linear form of the Poisson–Boltzmann equation to describe the radial decay of potential away from the charged surface; (2) exact location of the slip plane within the channel; and (3) the description of the zeta potential as a single value throughout the specimen. These assumptions are taken to approximate the conditions at a *real* solid/liquid interface, which may have nonhomogeneous structure and nonideal charge distribution, within both the solid and the liquid.

The assumption of laminar, parabolic flow in each cylindrical channel has been made to simplify the model. At the slow, creeping flow rates often employed in studies of bone electromechanics, laminar, parabolic flow in small tortuous, channels appears to be a good first order evaluation of the flow patterns. At much higher driving frequencies, this assumption may be a limiting condition as nonlaminar flow patterns are developed. Where this assumption is not valid, the mathematical form of the convective current density will not be so simply expressed (equation 37), however, the physical principles will still apply.

Limitations in the boundary conditions must be considered. We must determine if the surface tension pressures developed are large enough to insure the no-flow condition on the surfaces $y = \pm h$, as dictated by equation (22). This is discussed in the numerical evaluation in Part II of this paper (Salzstein and Pollack, 1987). We must also consider that the fluid at the surface may spread along the surface. Zisman (1964) indicates that a fluid will not spread along a surface if the interfacial free energy between the liquid and the atmosphere ($\Gamma_{l/a}$) is greater than the critical surface tension (Γ_c) of the solid surface. We consider a typical value on the order of 75 dyn cm^{-1} for $\Gamma_{l/a}$. Eriksson (1985) indicates that a measured value of Γ_c for bone has not been reported, but typical values for dentin and enamel, 45 and 46 dyn cm^{-1}, respectively, should be reasonable estimates for Γ_c for bone. Zisman's criteria would then indicate that spreading of fluid along the surface would not occur, supporting the development of surface tension pressures and the no-flow boundary condition.

Functional dependencies

The model is developed in terms of many parameters which have been investigated previously. These include the mechanical and electrical properties of both the fluid and the bone matrix and the size and distribution of the microporous spaces. The tortuosity of the pathways of the microporosity is not known, though studies of cartilage indicate that a value of 1–2 is appropriate for that tissue (Maroudas, 1973). Dullien (1979) indicates an appropriate range for tortuosity of 1–3 for many porous materials.

Equation (43) describes the electrokinetic response to deformation of the bending specimen shown in Fig. 1. Figures 4 and 5 indicate, in non-dimensional analysis, the effect of increasing frequency on the electrokinetic response. The second part of this paper investigates these dynamic characteristics experimentally.

Figure 4 predicts the voltage profile across the sample to be a relatively linear profile from the tensile side to the compressive side. Starkebaum *et al.* (1979) used a microelectrode technique to examine this type of voltage profile. Their results indicated an interesting profile across their bovine and human samples. The profile was specifically related to the osteonal architecture of the sample. The total voltage profile was composed of two components: (1) voltage 'cusps' around each Haversian canal, described as intraosteonal potentials or micro-SGPs; and (2) a linear voltage profile across the entire specimen. Pollack *et al.* (1984) addressed the intraosteonal potentials in an earlier paper. The linear profile is similar to the voltage profile described here.

The dynamic characteristics of the electrokinetic response of this model are determined by the product of the aggregate modulus H_A of bone and the permeability k associated with the microporosity. H_A can be evaluated from previous reports of mechanical properties of bone and the standard relationships among the elastic constants. The value of k is not simple to evaluate. Rouhana *et al.* (1981) have studied the permeability of cortical bone by driving fluid through macroscopic samples and measuring the fluid flow through the sample for a given pressure head, as dictated by Darcy's law. They report values of the order of 10^{-11} m^4 Ns^{-1} after clearing cellular debris in the vascular compartments in bone. This is not the same permeable compartment considered here since the true architecture of bone, with its vascular, lacunar and canalicular spaces, will dominate the permeability of the tissue in Rouhana's experiment. These compartments will act as shunts for the fluid to permeate. The microporosity, with channel sizes on the order of several hundred Ångstroms, will have a much smaller permeability than the values reported by Rouhana *et al.* (1981).

Equation (43) describes an inverse relationship between the SGP and the conductivity of bone. Chakkalakal *et al.* (1980) and Kosterich *et al.* (1984) determined that the conductivity of cortical bone is 0.5–1% of the conductivity of the fluid in which the bone is steeped. Gross and Williams (1982) and Pienkowski and Pollack (1983) measured the changes in SGP amplitude as a function of steeping solution conductivity and reported an inverse relationship, as predicted by equation (43).

Equation (43) also predicts an inverse relationship between SGP amplitude and viscosity of the steeping solution. This has also been found experimentally and reported by Gross and Williams (1982) and Pienkowski and Pollack (1983), for solutions of viscosity up to 100 times that of water.

The step response or time domain solution of this biphasic analysis results in the following equation describing the voltage decay across the sample

$$V_{SGP} = \frac{-32Z\varepsilon\phi^f Gh\mu_s}{3\pi^2\eta T^2\sigma_h}\left[\frac{I_2(\kappa\delta/2)}{I_0(\kappa\delta/2)}\right] \times \sum_{\substack{n=1 \\ \text{odd}}}^{\infty} \frac{\exp\left[-H_A k\left(\frac{n\pi}{2h}\right)^2 t\right]}{n^2}. \quad (52)$$

This is derived by solving equation (16) with $g(t)$ given by a step function rather than $Ge^{i\omega t}$ and with the boundary conditions dictated by equations (13) and (21) and the electrokinetic equations. G reflects the magnitude of the step deformation and equals the inverse of the radius of curvature of the bending plate. τ_n are time constants describing the decay of the voltage

$$\tau_n = \frac{96\eta}{H_A\phi^f}\left(\frac{hT}{n\pi R}\right)^2. \quad (53)$$

Equation (52) indicates that the voltage decay is described by multiple time constants, as typically found experimentally. Equation (52) predicts an SGP response to step loading, shown in Fig. 6, for a negative zeta potential. These are characteristic of the experimental SGPs described in the literature (Gross and Williams, 1982; Pienkowski and Pollack, 1983).

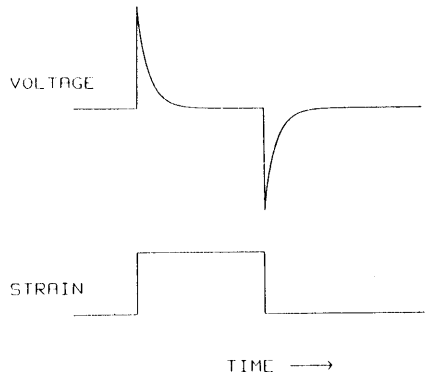

Fig. 6. SGP response to step deformation, as predicted by equation (52).

The time constants described in equation (53) are linearly related to solution viscosity, again found experimentally by Pienkowski and Pollack (1983). Also, the time constants are independent of solution conductivity, as reported by these two groups. Further numerical analysis is considered in Part II of this paper.

Experimental analysis of the model is reported in Part II of this paper for SGP amplitude and phase data as a function of frequency (Salzstein and Pollack, 1987). The excellent fit of the data to the functional form of equation (43) enables the determination of all model parameters for the bone specimens tested.

CONCLUSION

A continuum model has been developed to account for the electromechanical voltages (stress-generated potentials) developed across plates of cortical bone. Basic principles of electrokinetic theory and the biphasic analysis of porous materials allow the determination of induced streaming potentials. We neglect the specific architecture of the tissue in this approach and model the microporosity of bone as a continuum. Many of the experimental results reported to date are explained by this model. Quantitative evaluation of the model is presented in Part II of this paper. Low frequency testing of dynamic properties of stress-generated potentials presented in Part II indicate that it is the microporosity of bone that is the fluid compartment to consider in the generation of these potentials.

Acknowledgement—The authors acknowledge with great appreciation the support of the National Science Foundation (Grants ECS 84-11335 and INT 81-08481) and the Bulgarian Academy of Sciences for their continued support throughout this collaborative study.

REFERENCES

Armstrong, G., Lai, W. M. and Mow, V. C. (1984) An analysis of the unconfined compression articular cartilage. *J. biomech. Engng* **106,** 165–173.

Anderson, J. and Eriksson, C. (1968) Electrical properties of wet collagen. *Nature* **218,** 166–168.

Chakkalakal, D. A., Johnson, M. W., Harper, R. A. and Katz, J. L. (1980) Dielectric properties of fluid-saturated bone. *IEEE Trans. Biomed. Engng* **27,** 95–100.

Dullien, F. A. L. (1979) *Porous Media: Fluid Transport and Pore Structure.* Academic Press, New York.

Eriksson, C. (1976) Bone morphogenesis and surface charge. *Clin. Orthop.* **121,** 295–302.

Eriksson, C. (in press) Surface energies and the bone induction principle. *J. biomed. Mat. Res.*

Grodzinsky, A. J. (1983) Electromechanical and physiochemical properties of connective tissue. *CRC Crit. Rev. biomed. Engng* **9,** 133–199.

Gross, D. and Williams, W. S. (1982) Streaming potential and the electromechanical response of physiologically moist bone. *J. Biomechanics* **15,** 227–295.

Holmes, J. M., Davies, D. H., Meath, W. J. and Beebe, R. A. (1964) Gas adsorption and surface structure of bone mineral. *Biochemistry* **3,** 2019–2023.

Johnson, M. W. (1984) Behavior of fluid in stressed bone cellular stimulation. *Calcif. Tissue Int.* **36,** S72–S76.

Johnson, M. W., Chakkalakal, D. A., Harper, R. A. and Katz, J. L. (1980) Comparison of electromechanical effects in wet and dry bone. *J. Biomechanics* **13,** 437–442.

Kosterich, J. D., Foster, K. R. and Pollack, S. R. (1984) Dielectric properties of fluid saturated bone: effect of variation in conductivity of immersion fluid. *IEEE Trans. biomed. Engng* **31,** 369–374.

Lakes, R. S. and Katz, J. L. (1984) Viscoelastic properties of bone. *Natural and Living Biomaterials* (Edited by Hastings, G. W. and Ducheyne, P.), pp. 61–87. CRC Press, Boca Raton, FL.

Lee, R. C., Frank, E. H., Grodzinsky, A. J. and Roylance, D. K. (1981) Oscillatory compressional behavior of articular cartilage and its associated electromechanical properties. *J. biomech. Engng* **103,** 280–292.

Maroudas, A. (1973) Physiochemical properties of articular cartilage. *Adult Articular Cartilage* (Edited by Freeman, M. A. R.), pp. 131–170. Grune and Stratton, New York.

Moore, W. J. (1972) *Physical Chemistry.* Prentice-Hall, Englewood Cliffs, NJ.

Mow, V. C., Kuei, S. C., Lai, W. M. and Armstrong, C. G. (1980) Biphasic creep and stress relaxation of articular cartilage in compression: Theory and experiments. *J. biomech. Engng* **102,** 73–84.

Mow, V. C. and Lai, W. M. (1980) Recent developments in synovial joint biomechanics. *SIAM Rev.* **22,** 275–317.

Neuman, W. F. and Neuman, M. W. (1958) *The Chemical Dynamics of Bone Mineral.* University of Chicago Press, Chicago.

Pienkowski, D. and Pollack, S. R. (1983) The origin of stress-generated potentials in fluid saturated bone. *J. orthop. Res.* **1,** 30–41.

Pollack, S. R., Petrov, N, Salzstein, R., Brankov, G. and Blagoeva, R. (1984) An anatomical model for streaming potentials in osteons. *J. Biomechanics* **17,** 627–636.

Rouhana, S. W., Johnson, M. W., Chakkalakal, D. A., Harper, R. A. and Katz, J. L. (1981) Permeability of compact bone. *ASME biomech. Symp.* **AMD-43,** 169–172.

Salzstein, R. and Pollack, S. R. (1987) Electromechanical potentials in cortical bone. Part II: Experimental analysis. *J. Biomechanics* **20,** 271–280.

Scheidegger, A. E. (1974) *The Physics of Flow Through Porous Media.* University of Toronto Press, Toronto.

Shaw, D. (1969) *Electrophoresis.* Academic Press, New York.

Starkebaum, W. S., Pollack, S. R. and Korostoff, E. (1979) Microelectrode studies of stress generated potentials in four point bending of bone. *J. biomed. Mat. Res.* **113,** 729–751.

Yasuda, I. (1953) Fundamental aspects of fracture treatment. *J. Kyoto Med. Soc.* **4,** 395–406.

Zisman, W. A. (1964) Relation of the equilibrium contact angle to liquid and solid constitution. *Adv. Chem. Ser.* **43,** 1–51.